Supporting Information for

Comparison of Particle Number Emissions from In-Flight Aircraft Fueled with Jet A1, JP-5 and an Alcohol-to-Jet Fuel Blend

*Steven Tran[1], Anthony Brown[2], Jason S. Olfert[1]**

[1]Department of Mechanical Engineering, University of Alberta, Edmonton, AB, Canada

[2]NRC Aerospace, National Research Council Canada, Ottawa, ON, Canada

**Corresponding Author*

Number of pages: 25

Number of figures: 14

Number of tables: 4

S1 Particle Transport and Counting Efficiency in the Isokinetic Sampling System and Particle Counters

S1.1. Introduction

This section of the supporting information details the calculation of the transport losses and resulting counting efficiencies of the two CPCs. Particle losses through the sampling lines are important because it will affect the particle concentrations measured by the CPCs resulting in fewer particles detected by the CPCs than actual particles in the sample flow. The counting efficiencies of the CPCs can also be affected as particles below a certain size may not be able to fully penetrate the sampling lines which increases the 'effective' cut-off diameters of the CPCs.

S1.2. Particle Transport Efficiency through the Sampling System

A schematic of the isokinetic sampling system of the National Research Council Canada (NRC) CT-133 jet aircraft is shown in Figure S1. The sample flow enters the system through an isokinetic probe which consists of a conical tip and a bent tube (Section 1). The conical tip is attached to a stainless-steel tube comprised of a straight length and a 90° bend. The sample flow subsequently enters a coupler after the first section, which has a 90° elbow. The flow is then directed through Section 2 of the sampling system consisting of a conductive flexible tube that is bent at two points with bending angles of 20° and −20°. The sample is drawn through a manifold, where a small fraction of the sample is directed towards the lines leading to both particle counters and the rest of the sample flows to the mass flow controller and bulkhead exhaust. After the manifold, the sample enters Section 3 which consists of an elbow and a straight stainless-steel tubing connected to an additional length of flexible conductive tubing leading to a Y fitting that splits the sample flow to both condensation particle counters (CPC). Section 4 leads the sample to the TSI Model 7610 CPC. Section 5 leads to a second Y fitting which splits the flow between the catalytic denuder and the bypass line to the TSI Model 3776 CPC. Both Sections 6 and 7 contain pinch valves that are used to control whether the sample goes through the catalytic denuder (Section 6) to measure non-volatile particles or the bypass line (Section 7) to measure total particles. Section 8 is the last

section of the particle sampling system which leads the sample to the TSI Model 3776 CPC. Table S1 shows a summary of the total lengths and inner diameters for each section.

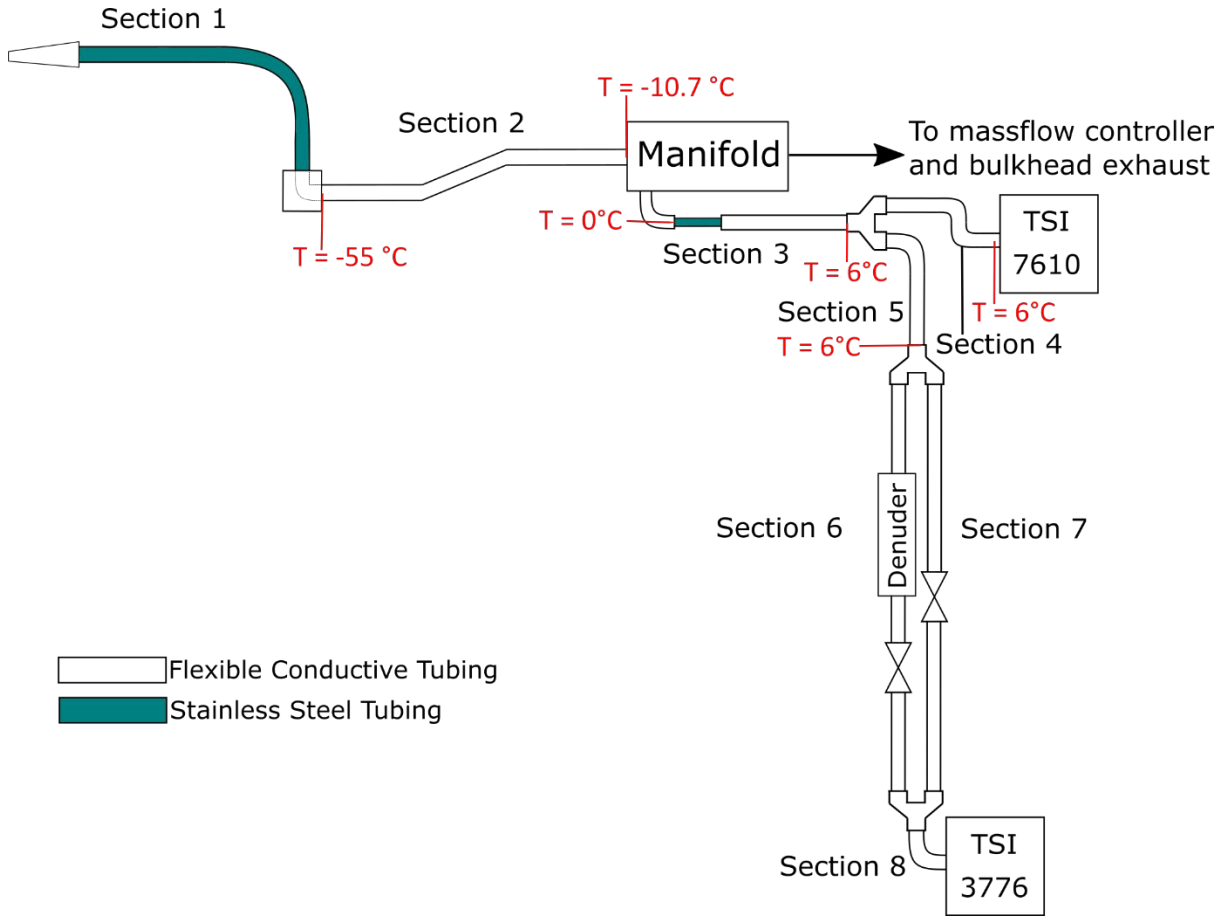

Figure S1. Schematic of the particle sampling system.

Particle losses in the system will be a function of the particle size. We assume contrail particles that will be measured by the system will consist of a small soot particle core (with diameter less than 100 nm) and a shell of frozen water at very low temperatures at high altitudes. Therefore, it is important to consider the effect of pod temperature on the sampled particles and their estimated size as they enter the particle counter. It is known from previous experimental conditions that at top-of-climb, the pod temperature is ~20 °C and at top-of-descent, the pod temperature is ~6 °C. A pod temperature of 6 °C is considered in this study as the worst-case scenario for the effect of temperature on sampled particles. A heat transfer analysis was conducted on flow temperature as it traveled through the sampling system.

Figure S1 shows the estimated flow temperature for various sections of the sampling system which are also summarized in Table S1. The flow temperature also affects air properties, such as density, viscosity, and volumetric flow rate, in different sections of the sampling system which, in turn, affect particle loss. Figure S1 shows that up to the manifold, the flow temperature is below zero and the water in the contrail particles will not evaporate; however, at the beginning of Section 3, the flow temperature reaches zero and increases up to 6 °C (*i.e.* pod temperature) at the end of that tube. Calculations show that the residence time of particles in Section 3 is much larger than their evaporation time. Therefore, particles reach the particle counter as soot with no condensed water vapour on them.

Three mechanisms for particle loss in the sampling system are considered: Diffusion loss in the tubes, inertial deposition loss in the bends and losses through the catalytic denuder. The extent of particle loss in each mechanism depends on the flow regime in the probe. Therefore, Reynolds number is an important parameter to consider when calculating particle loss in the probe. Because eddies do not form in expansions with a half angle less than 4°, inertial deposition particle loss is negligible in the conical tip[1]. However, diffusion loss must be still considered for the conical tip.

Figure S1 also shows a simplified model of the actual sampling system for the estimation of particle losses. As it will be shown later, diffusion losses depend on tube length; therefore, the overall length of conical tip and the bent tube was considered as 610 mm for diffusion loss calculations. The overall straight section of the stainless-steel tube was 330 mm long, which was used to estimate inertial deposition losses in straight tubes.

Based on flight data, it was assumed that the isokinetic probe was at ambient conditions of −55 °C and 23 kPa. The rest of the sampling system was in a heated pod at 6 °C; however, it took some time for the sampled flow to heat up to the pod temperature. In the particle loss analysis, the flow temperature was assumed to be −55 °C in Section 1, –an average of −33 °C in Section 2, and average of 3 °C in Section 3, and 6 °C in Sections 4 to 8. The density and viscosity of the air was calculated based on the temperature

in each section. Assuming that the mass flow controller regulated the volumetric flow rate at 25 litres per minute at ambient pressure and temperature, Reynolds number was calculated to be 1,274 and 1,326 in Section 1 and Section 2, respectively. Therefore, the flow was laminar in both Sections 1 and 2. The particle counters both drew in a volumetric flow rate of 1.5 L/min (at 23 kPa and 6 °C) via their own pump. Thus, the Reynolds number in the stainless-steel tube and the conductive tubing of Section 3 was 166 and 110, respectively. The Reynold's number in Sections 4 to 8 was 55 and, therefore, the flow regime in all the remaining sections was laminar as well.

Table S1. Summary of each section of the sampling system

Section	Total length (mm)	ID (mm)	Flowrate (L/min)	Temperature (°C)	Reynolds number
1	610	10.7	25	-55	1274
2	483	9.5	25	-33	1326
3 (Steel)	190.5	4.3	3	3	166
3 (Conductive tubing)	165	9.5	3	6	110
4	76	9.5	1.5	6	55
5	210	9.5	1.5	6	55
6	585	9.5	1.5	6	55
7	832	9.5	1.5	6	55
8	127	9.5	1.5	6	55

S1.2.1. Diffusion Loss

Kulkarni et al.[1] suggests the following set of equations to calculate transport efficiency (*i.e.* penetration) due to diffusional loss:

$$P_{\text{diff}} = \exp\left(-\xi \cdot Sh\right) \tag{S1}$$

$$\xi = \frac{\pi D L}{Q} \tag{S2}$$

where L is the tube length, Q is the volumetric flow rate, and D is the particle diffusion coefficient. Sherwood number, Sh, for laminar flow is calculated by the following empirical equation

$$\text{Sh}_{\text{laminar}} = 3.66 + \frac{0.0668\frac{d}{L}\text{Re} \cdot \text{Sc}}{1 + 0.04\left(\frac{d}{L}\text{Re} \cdot \text{Sc}\right)^{2/3}} \tag{S3}$$

Reynolds number, Re, and Schmidt number, Sc, in Eq. S3 is defined as

$$\text{Re} = \frac{\rho U d}{\mu} \tag{S4}$$

$$\text{Sc} = \frac{\mu}{\rho D} \tag{S5}$$

where d is the inner tube diameter. Particle diffusion coefficient, D, is defined by

$$D = \frac{kTC_{\text{c}}}{3\pi\mu d_{\text{p}}} \tag{S6}$$

where, C_{c} is the Cunningham slip correction factor (significant for particles in the range of or smaller than the mean free path of the air molecules) and d_{p} is the particle diameter. The mean free path of air molecules, λ, was calculated using[2]

$$\lambda = \lambda_0 \left(\frac{T}{T_0}\right)\left(\frac{P_0}{P}\right)\left(\frac{1+\frac{S}{T_0}}{1+\frac{S}{T}}\right) \quad \text{(S7)}$$

where P is the pressure, T is the temperature, S is the Sutherland constant (S = 110 K for air)[2] and λ_0, P_0 and T_0 are the reference mean free path, pressure and temperature respectively. At a reference temperature and pressure of T_0 = 293.15 K and P_0 = 101.3 kPa, the mean free path is λ_0 = 0.0665 μm.[1] At a pressure of 23 kPa and temperatures of -55 °C and 6 °C, the mean free path of air molecules was estimated to be ~199 nm and ~275 nm, respectively. The Cunningham slip correction factor was calculated using[1]

$$C_c = 1 + \frac{\lambda}{d_p}\left(2.33 + 0.966\exp\left(-0.499\frac{d_p}{\lambda}\right)\right) \quad \text{(S8)}$$

S1.2.2. Inertial Deposition in the Bend

Pui et al.[3] gives the following empirical relation for inertial deposition in a laminar flow through a bend:

$$P_{\text{depos, laminar, bend}} = \left(1 + \left(\frac{Stk}{0.171}\right)^{0.452\left(\frac{Stk}{0.171}\right)+2.242}\right)^{-\frac{2}{\pi}\theta} \quad \text{(S9)}$$

$$\text{Stk} = \frac{\tau U}{d} \quad \text{(S10)}$$

where Stk is the Stokes number and θ is the angle of the bend in radians. In Eq. S10, τ is the relaxation time, U is the flow velocity and d is the tube diameter.

S1.2.3. Losses in the Catalytic Denuder

The losses in the Catalytic Instruments, Model CS015 denuder was modeled by using the provided equation in the instrument manual,[4]

$$P = \left(x_1 e^{-\frac{x_2}{d_p^2}} + x_3 e^{-\frac{x_4}{d_p^2}} \right) x_5 \quad \text{(S11)}$$

where d_p is the particle diameter (in nm) and $x_1 - x_5$ are fitting parameters with the values shown in Table S2.

Table S2. Fit parameters for Equation S11

Parameter	Value
x_1	0.190
x_2	499
x_3	0.925
x_4	36.0
x_5	0.670

The resulting penetration efficiency curve is shown in Figure S2. As can be seen in Figure S2, the catalytic denuder has a maximum penetration efficiency of 75% once particles reach 100 nm or larger.

Therefore, the measurement of non-volatile particles will experience a large amount of losses due to the denuder.

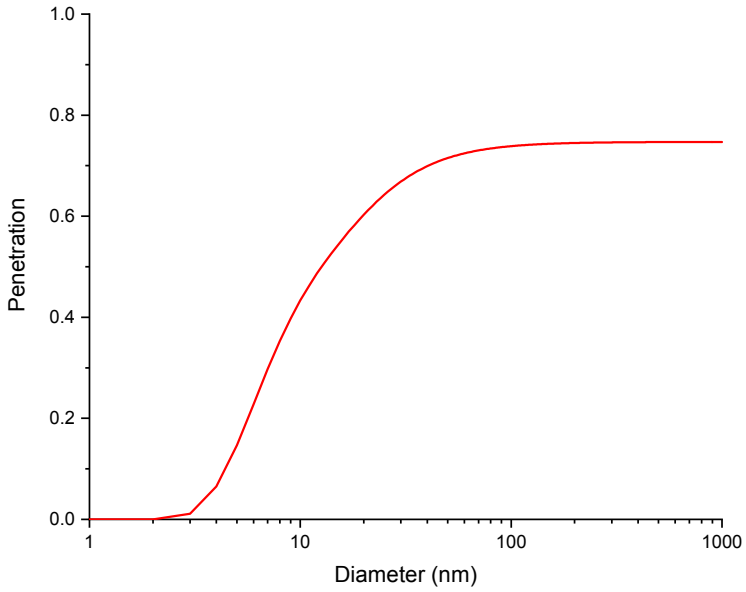

Figure S2. Penetration efficiency of particles in the catalytic denuder.

S1.3. Counting Efficiency of the Particle Counters

The cut-off diameters of the counting efficiency of the TSI 3776 CPC and TSI 7610 CPC were found by fitting data provided in the TSI Model 3776 manual[5] and data estimated from Zhang and Liu[6] for standard condition operation; respectively. A sigmoidal logistic fit was applied with the form shown in Eq. S12 and the parameters for both CPCs are shown in Table S3.

$$y = \frac{1}{1 + e^{-k(x - x_c)}} \tag{S12}$$

Table S3. Parameters for logistic fit for both CPCs.

Parameters	TSI 3776	TSI 7610
k	7.11741	0.38999

x_c	2.27708	14.82943

132

133 The resulting counting efficiencies of the TSI 3776 CPC and the TSI 7610 CPC are shown in Figure
134 S3. The 3776 CPC also has a much smaller cut-off diameter, d_{50}, of 2.5 nm compared to the 7610 CPC d_{50}
135 of approximately 15 nm.

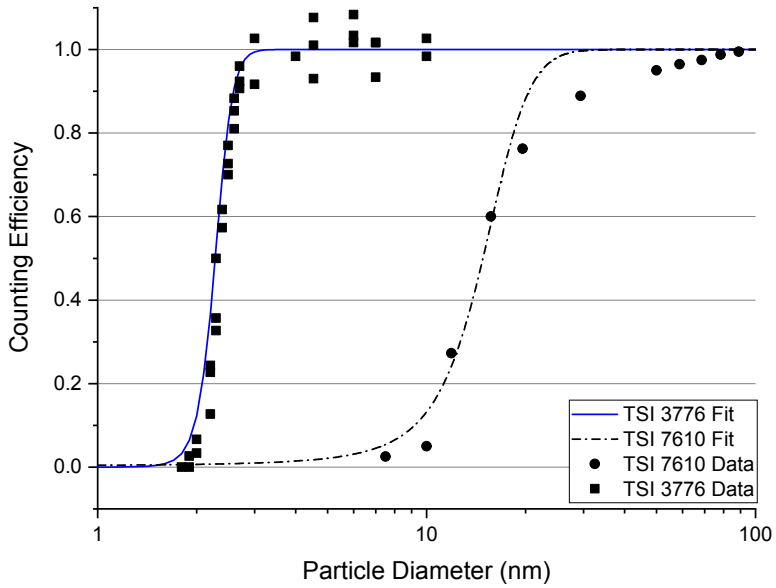

136

137 **Figure S3.** Counting efficiency of TSI 3776 and 7610 CPCs.

138

139 **S1.4. Overall Counting Efficiency of the Sampling System and Particle Counters**

140 The overall penetration of particles through the sampling system takes into account the three different
141 particle loss mechanisms in each tube section and bends, the catalytic denuder as well as the counting
142 efficiency of the CPCs and was calculated using

$$P_{\text{overall}} = \frac{n_{\text{out}}}{n_{\text{in}}} = P_{\text{diff}} \times P_{\text{depos, bend}} \times P_{\text{denuder}} \times P_{\text{CPC}} \quad \text{(S13)}$$

143 This assumes that the particle concentration is uniformly distributed across the tube at the entrance to
144 each section.

145 **S1.5. Results**

146 Figure S4 shows the overall penetration of particles through the system before reaching the CPCs. It
147 can be seen that with the current geometry, particle losses in the lines leading to the TSI 7610 CPC are the
148 lowest with a d_{50}, the diameter where the penetration efficiency is less than 50%, of 3.5 nm. For the
149 bypass line leading to the TSI 3776 CPC, the d_{50} is slightly larger at 7.7 nm. Finally, the catalytic denuder
150 has the largest impact on the penetration efficiency by reducing the maximum penetration efficiency to
151 75%, which leads to the largest d_{50} of 13.3 nm.

152 It should be noted that particle loss is negligible for the straight sections because the flow regime is
153 laminar. Nevertheless, particle loss due to deposition in bends is still important mainly for particles larger
154 than 10 μm. We expect particles in Sections 1 and 2 of the sampling system to contain contrail particles
155 larger than 1 μm because these sections are not sufficiently warm to evaporate the condensed water;
156 however, deposition loss in the bends is negligible for particle sizes up to 3 μm. Therefore, diffusional
157 losses are the most significant contributor to the penetration efficiency of most particles through the
158 sampling system. Due to the higher temperature of the flow in Sections 3–8, all water will evaporate and
159 only soot particles survive, which generally have a median size less than 100 nm[7,8]. As seen in Figure S4,
160 the sections leading to the TSI 7610 CPC and the bypass line leading to the TSI 3776 CPC have
161 negligible particle losses for particles larger than 100 nm but the penetration efficiency begins to drop as
162 the particle diameter decreases. As mentioned, the line including the catalytic denuder and leading to the
163 TSI 3776 CPC has a penetration efficiency of 75% and has greater particle losses compared to the other
164 two lines.

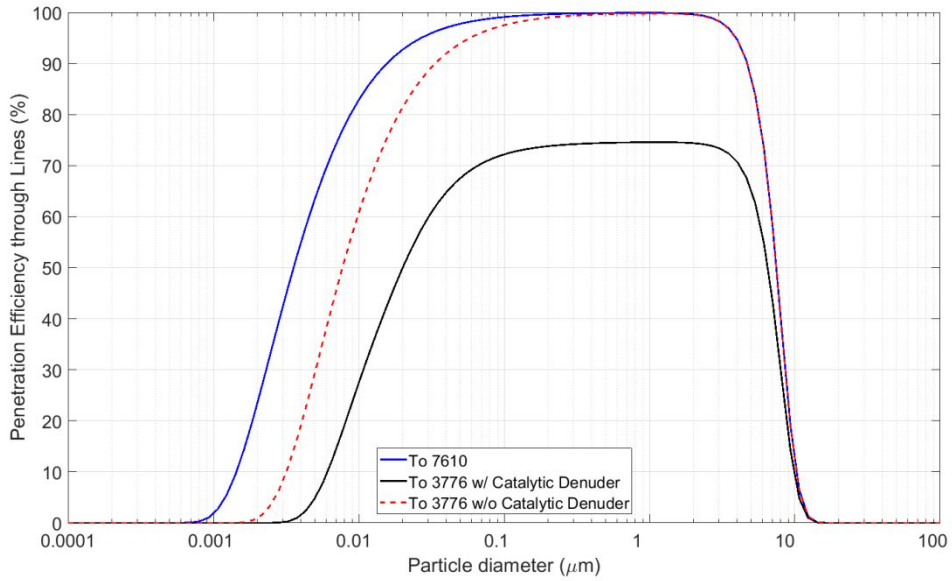

Figure S4. Overall particle penetration efficiency in the sampling system before the CPCs

Figure S5 shows the total counting efficiency of the sampling system including the counting efficiency of the CPCs. The resulting effective d_{50} of the TSI 3776 CPC and sampling system became 7.7 nm and 13.3 nm for the bypass line and catalytic denuder line, respectively. On the other hand, the effective d_{50} of the TSI 7610 CPC and sampling system remained relatively unchanged at 15.4 nm.

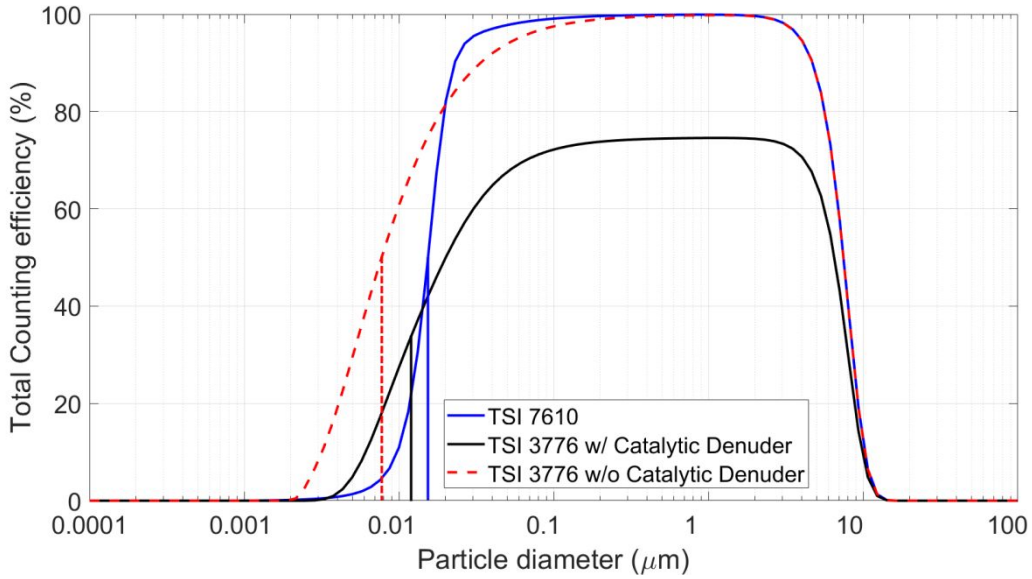

Figure S5. Total overall counting efficiency as measured by the CPCs.

S2 Uncertainty Calculation

As shown in the manuscript, the calculation of the ratio of particle emissions indices was determined by:

$$EI_{\mathrm{Ratio}} = \frac{EI_{\mathrm{N_{Alt}}}}{EI_{\mathrm{N_{Jet\ A1}}}} = \frac{\left(\frac{N - N_{\mathrm{bg}}}{P_{\mathrm{CPC}} \times \left(y_{\mathrm{NO_x}} - y_{\mathrm{NO_{xbg}}}\right)}\right)_{\mathrm{Alt}}}{\left(\frac{N - N_{\mathrm{bg}}}{P_{\mathrm{CPC}} \times \left(y_{\mathrm{NO_x}} - y_{\mathrm{NO_{xbg}}}\right)}\right)_{\mathrm{Jet\ A1}}} \quad \text{(S14)}$$

A Monte Carlo simulation was done using the bias uncertainties for the particle number, N, background particle number, N_{bg}, NO_x concentration, y_{NOx}, and the NO_x background concentration, y_{NOxbg}. The uncertainty in the CPC pressure, P_{CPC}, was assumed to be negligible because the uncertainty in N was expected to be much larger. The precision uncertainty was accounted for by combining multiple segments from the same flight where possible. For each segment (or flight) a Monte Carlo simulation was performed where the top and bottom parts of Eq. S14 were calculated separately 10,000 times and were then used to calculate 10,000 ratios. Since the same instrument was used for both the alternate and Jet A1 fuel measurements, by taking the ratio, the bias uncertainties would ideally cancel out (ie. There would be no uncertainty in the particle number, N, and NO_x concentration, y_{NOx}.). By including the uncertainties for N and y_{NOx}, a worst case scenario is being assumed where there is some variation in the performance of the instruments during the back-to-back measurements of the exhaust plumes from the different fuels.

The uncertainty in the TSI 7610 CPC was taken from the manufacturer's specifications and was assumed to have a Gaussian distribution with $2\sigma = \pm 10$ % of reading for the Monte Carlo simulation. The TSI 3776 CPC on the other hand was assumed to have an uncertainty with a Gaussian distribution with $2\sigma = \pm 30$ % of reading. This higher value was chosen instead of the manufacturer specified 10% because a study by Takegawa et al.[9] found that the 3776 CPC overestimated particle concentrations by 20–40% for particles with mobility diameters of 11 and 48 nm at absolute inlet pressures of 102 and 60 kPa. Also, in one flight segment (Dec 21 with Jet A1 fuel) the CPC concentration sometimes reached concentrations

near 1x10^6 where coincidence error also increases. Thus, the increased uncertainty (2σ=±30 % of reading) is chosen to account for errors due to low pressure operation and coincidence.

The uncertainty in the background was calculated by taking half of the difference between the minimum and maximum background value immediately before or after the test section, represented as $\varepsilon_{N_{\mathrm{bg}}}$. The background concentration is not expected to be constant throughout the atmosphere may be changing during the flights. A square distribution was used for the background uncertainty as it was assumed that there was an equal chance for the background value to fall anywhere between the upper and lower limits.

In the past, NRC had calibrated the Thermo 42i NO_x analyzer over a range of NO_x concentrations and ambient pressures and provided the following calibration equations:

$$y_{\mathrm{NO_x}} = f_1(P)x + f_2(P) \tag{S15}$$

$$f_1(P) = \left(-4.39 \times 10^{-7}\right)P^3 + \left(3.35 \times 10^{-4}\right)P^2 - \left(9.13 \times 10^{-2}\right)P + 9.58 \tag{S16}$$

$$f_2(P) = \left(7.87 \times 10^{-7}\right)P^3 - \left(4.85 \times 10^{-4}\right)P^2 + \left(9.3010^{-2}\right)P - 4.98 \tag{S17}$$

where x is the measured NO_x concentration and P is the ambient pressure in mmHg. Eq. S16 and S17 were trend lines fitted to data for the slopes (response factor) and intercepts (zero offset) of the instrument response at different pressures. These equations were applied to the measured NO_x concentrations before being used to calculate the particle number emission index ratio. The uncertainty in the calibration becomes:[10]

$$\varepsilon_y^2 = \left(\frac{\partial y\,\partial f_1}{\partial f_1\,\partial P}\right)^2 \varepsilon_{f_1}^2 + \left(\frac{\partial y\,\partial f_2}{\partial f_2\,\partial P}\right)^2 \varepsilon_{f_2}^2 + \frac{\partial y^2}{\partial x}\,\varepsilon_x^2 \tag{S18}$$

where ε_{f_1} and ε_{f_2} are the uncertainties in Eq. S16 and S17 respectively. The values for ε_{f_1} and ε_{f_2} were determined by finding the largest difference between the trend lines and actual data points and were found

212 to be 4.34×10^{-3} and 7.65×10^{-2}, respectively. The calibration curves are shown in Figure S6 and Figure
213 S7. The uncertainty in the measured NO_x concentration, ε_x was taken as the uncertainty of the calibration
214 gas used for the calibration of the Thermo 42i NO_x analyzer (ε_x = 1%). The uncertainty in the measured
215 NO_x concentration, $\varepsilon_{y_{NO_x}}$, was then calculated using Eq. S18. For the test conditions in this study $\varepsilon_{y_{NO_x}}$
216 ranged between 1.3% and 1.4%. In the Monte Carlo analysis, it was assumed that this uncertainty was
217 Gaussian.

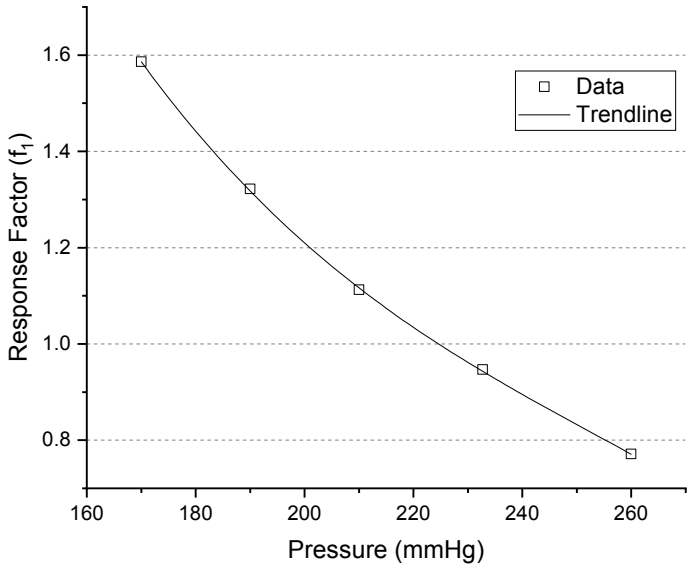

218

219 **Figure S6.** The NO_x calibration response factor as a function of pressure.

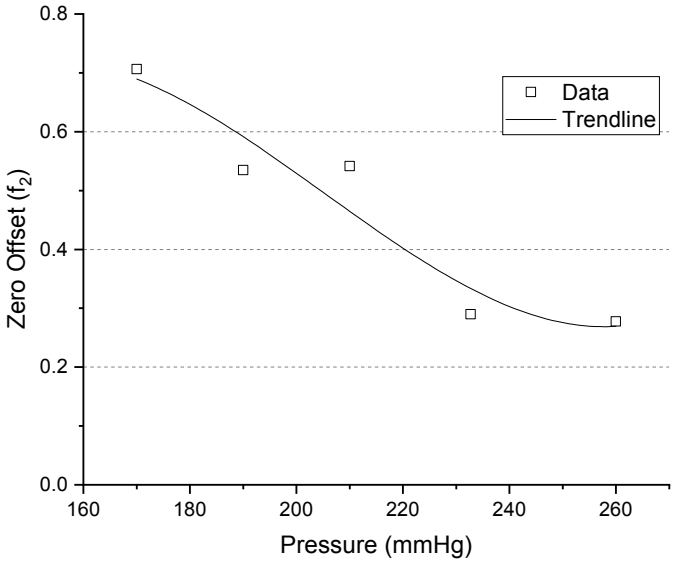

220

221 **Figure S7.** The NO_x calibration zero offset as a function of pressure.

222 The NO_x background uncertainty was determined by taking half of the difference between the
223 minimum and maximum of the trend lined fitted to the approximated background data. Thus, a square
224 distribution was used for the Monte Carlo simulation.

225 Sample histograms plots for the particle and NO_x concentration and background results for one segment
226 of the Dec 21 Jet A1 flight are shown in Figure S8. Only sample inputs for one type of fuel is shown
227 because all fuels had similar inputs.

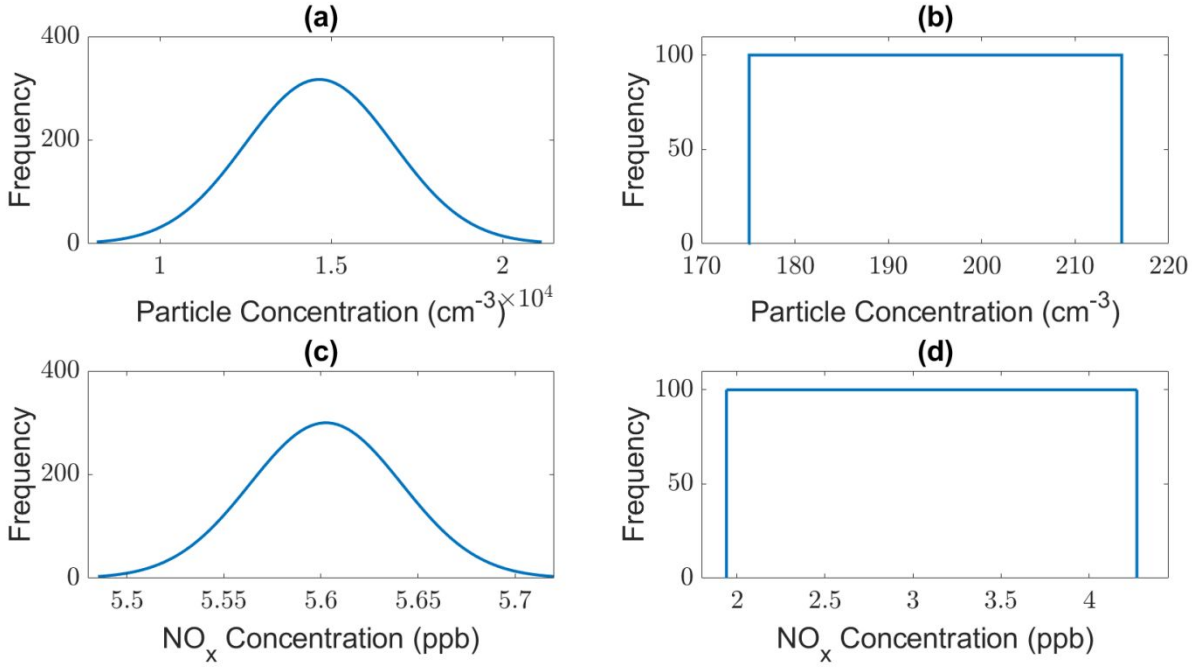

Figure S8. Sample inputs for the Monte Carlo Simulation for one segment of the Dec 21 Jet A1 flight (alternative fuels had similar inputs as well); (a) particle number concentration (TSI 3776), (b) background particle concentration (TSI 3776), (c) NO_x concentration and (d) background NO_x concentration.

For the Nov 20 flight, the ratio of particle emission indices between JP-5 and Jet A1 were determined. The resulting histogram plots and cumulative distribution plots for the particle emission index ratios of JP-5/Jet A1 from the 3776 CPC and 7610 CPC are shown in Figure S9. By using the cumulative distribution plots, the upper and lower limits were taken at the 95% and 5% levels respectively.

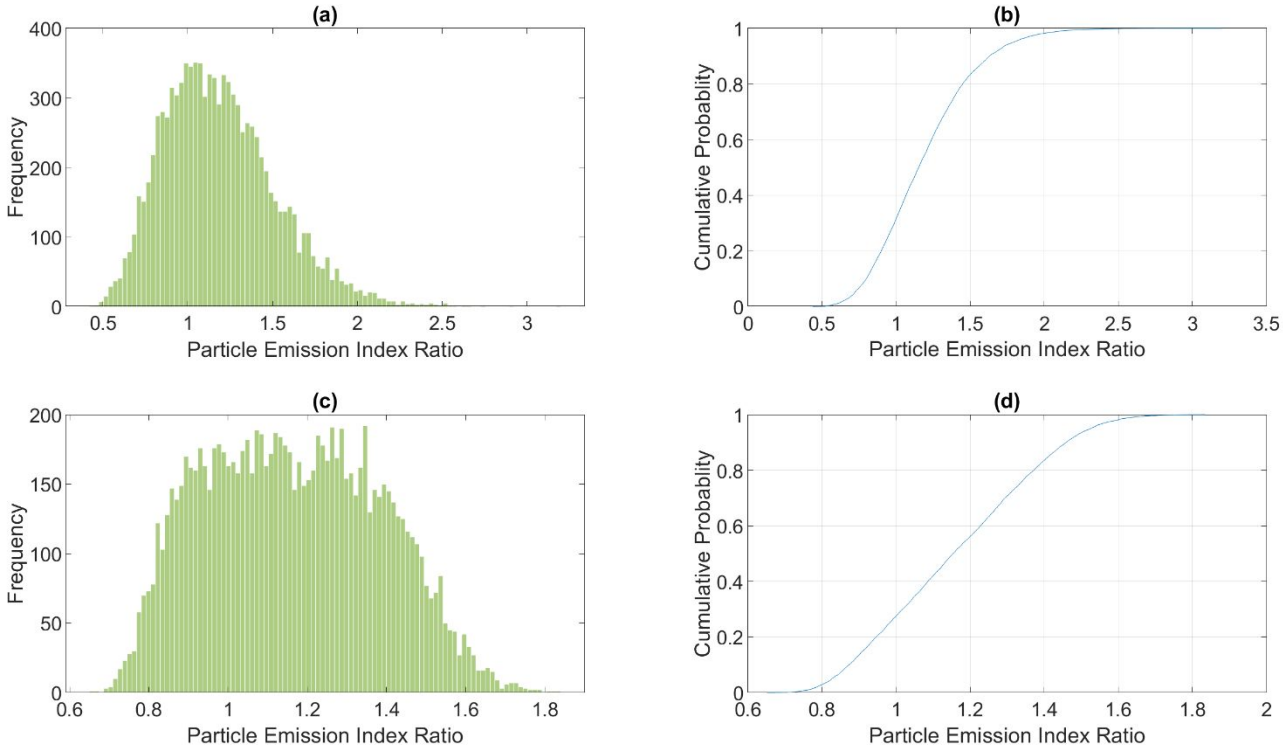

Figure S9. Monte Carlo results for Nov 20 total particle emission index ratio. (a) distribution for the TSI 3776 (b) cumulative distribution for the TSI 3776 (c) distribution for the TSI 7610 (d) cumulative distribution for the TSI 7610

The Dec 21 flights included a total of 2 separate denuded and non-denuded segments for the ATJ-SPK blend fuel case and 1 of each denuded and non-denuded segments for the Jet A1 case. For the 2 denuded and non-denuded segments of the ATJ-SPK blend fuel case, the average of the two separate segments was first taken before a ratio was calculated. A summary of the results for all cases is shown in Table S4.

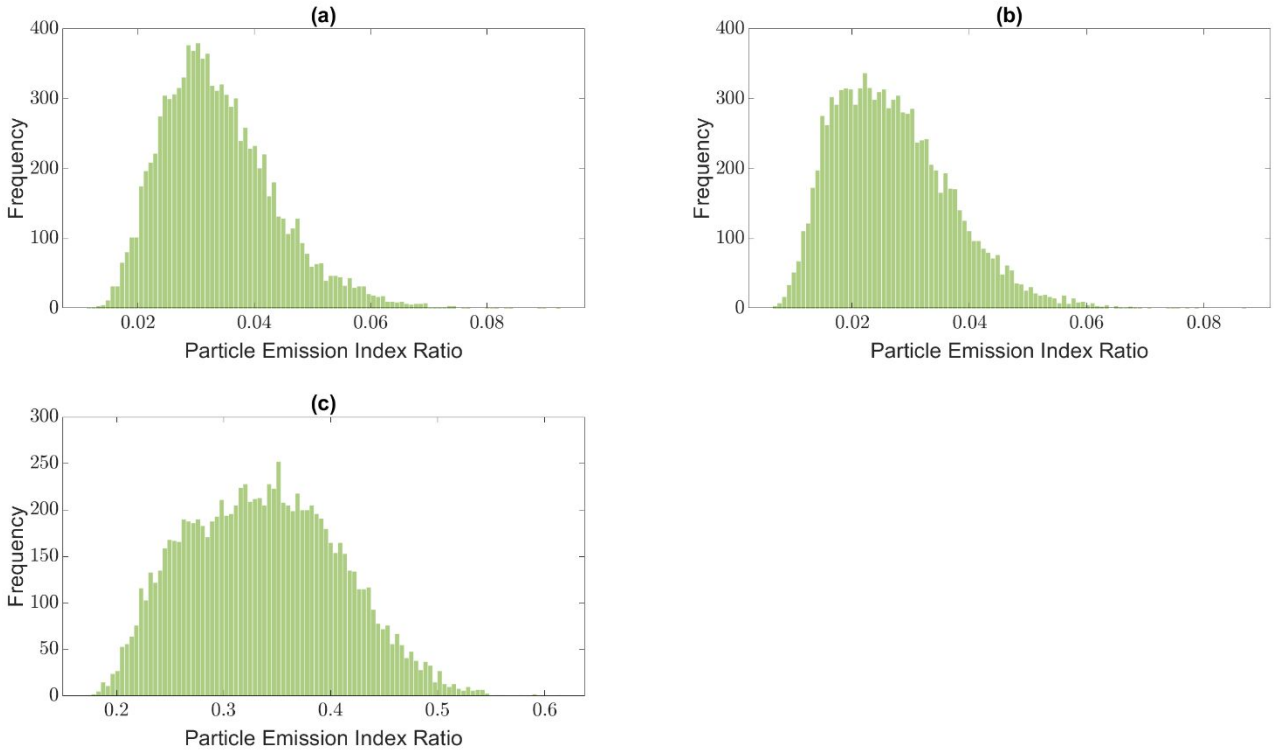

Figure S10. Monte Carlo results for Dec 21 flight particle emission index ratio between ATJ and Jet A1. (a) distribution for total particles from the TSI 3776 (b) distribution for total particles from the TSI 7610 (c) distribution for non-volatile particles from the TSI 3776.

Table S4. Summary of the final particle number emission index ratios for the CAAFCEB campaign. The particle number emission index ratios were calculated using integrals and the confidence intervals were determined from the Monte Carlo simulation

Flight Day	Fuel Types	Particle Type	Effective Cut-Off Diameter (nm)	Particle Number Emission Index Ratio	Uncertainty Upper limit (95%)	Uncertainty Lower limit (95%)
Nov 20	JP-5/Jet A1	Total	7.7	0.96	1.80	0.71
Nov 20	JP-5/Jet A1	Total	15.4	0.96	1.53	0.83
Dec 21	ATJ/Jet A1	Total	7.7	0.033	0.052	0.021
Dec 21	ATJ/Jet A1	Total	15.4	0.34	0.46	0.12
Dec 21	ATJ/Jet A1	Non-Volatile	13.3	0.030	0.045	0.013

S3 Raw data sample

Sample raw data plots for all flights are shown in Figure S11 to Figure S14. The highlighted sections represent the segments that were analyzed: red represent when the by-pass line was used to measure total particles and blue represents when the denuder was used to measure non-volatile particles. First data from the forward scattering spectrometer probe (Particle Measuring Systems Inc., FSSP-100) was used to identify when the CT-133 was in the contrails of the Falcon 20. Then the data for the particle and NO_x concentration was examined to determine periods where the concentrations were above background which meant that the exhaust plume was being sampled. The status of the catalytic denuder was also recorded and used to determine when it was in-line or when the bypass line was used. The altitude data was used as a reference to identify when the CT-133 was at a steady altitude (thus at cruise) in the contrail of the Falcon 20.

As seen in Figure S11 to Figure S14, the particle concentrations varied between high and low concentrations as the CT-133 flew in and out of the contrails. As shown in the figures, the NO_x concentrations have broader peaks and do not appear to vary at the same rate as the particle concentrations. This is due to the two CPCs having much faster response times (a little less than 1 second and 2 seconds for the TSI 3776 and TSI 7610 CPC; respectively) than the NO_x analyzer (tens of seconds for the Thermo 42i). Thus, in the analysis of the particle number emission index ratios, the integrals of the particle and NO_x concentrations over each segment was used instead of individual data points similar to the method of Schulte P. et al. (1997).[11]

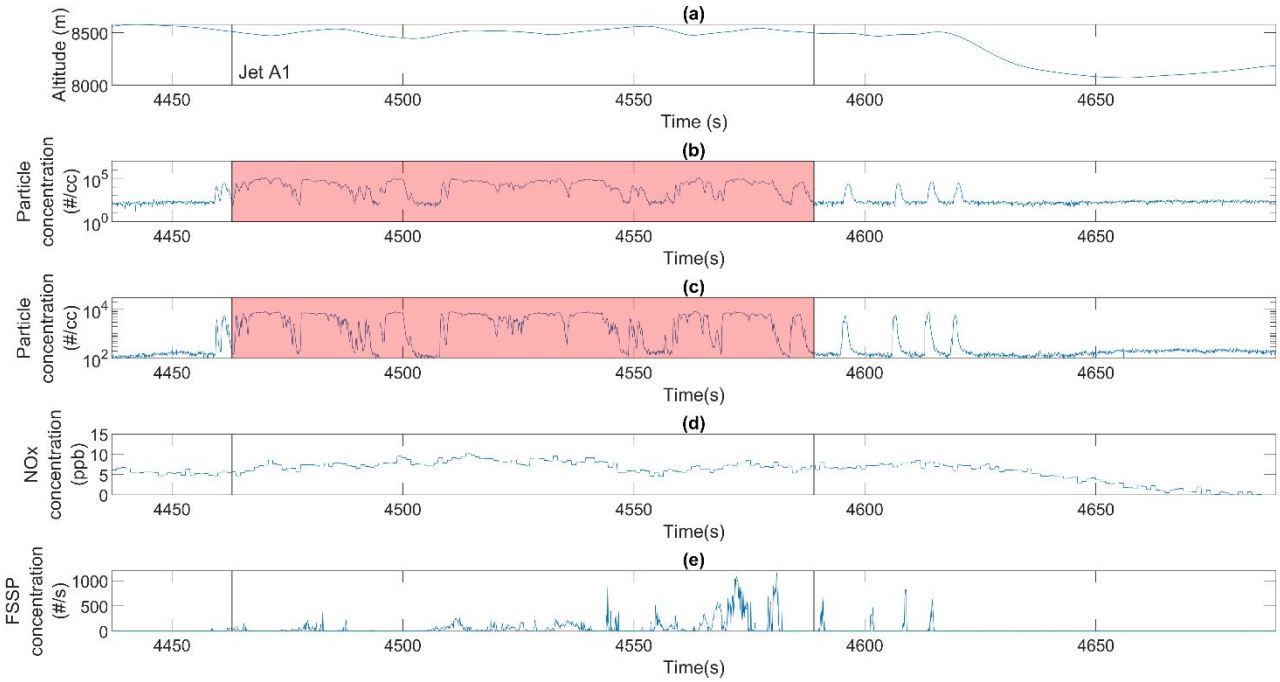

271

272 **Figure S11.** Raw data plot for the Jet A1 flight on Nov 20 with lines indicating the segments
273 chosen for analysis: (a) altitude measurements from the CT-133 (b) 3776 CPC particle
274 concentration, (c) 7610 CPC particle concentration, (d) NO_x concentration, (d) ice particle
275 concentration.

276

277

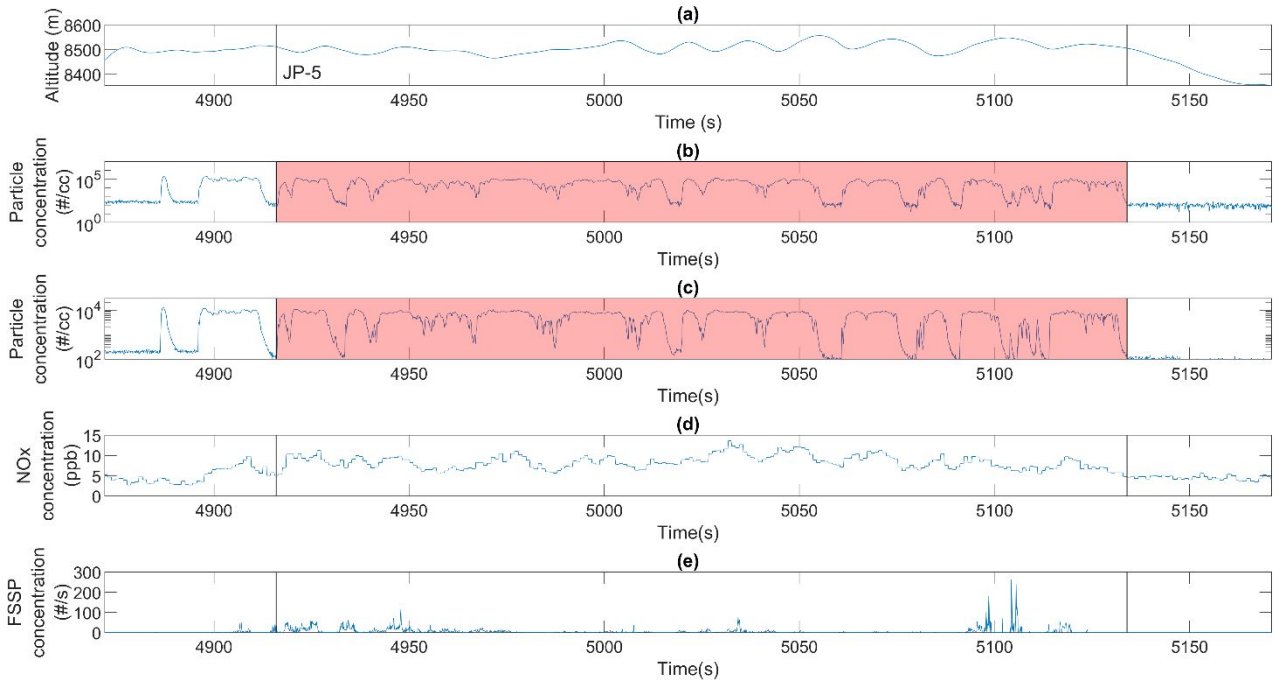

278

279 **Figure S12.** Raw data plot for the JP-5 flight on Nov 20 with lines indicating the segments
280 chosen for analysis: (a) altitude measurements from the CT-133 (b) 3776 CPC particle
281 concentration, (c) 7610 CPC particle concentration, (d) NO_x concentration, (d) ice particle
282 concentration.

283

284

285

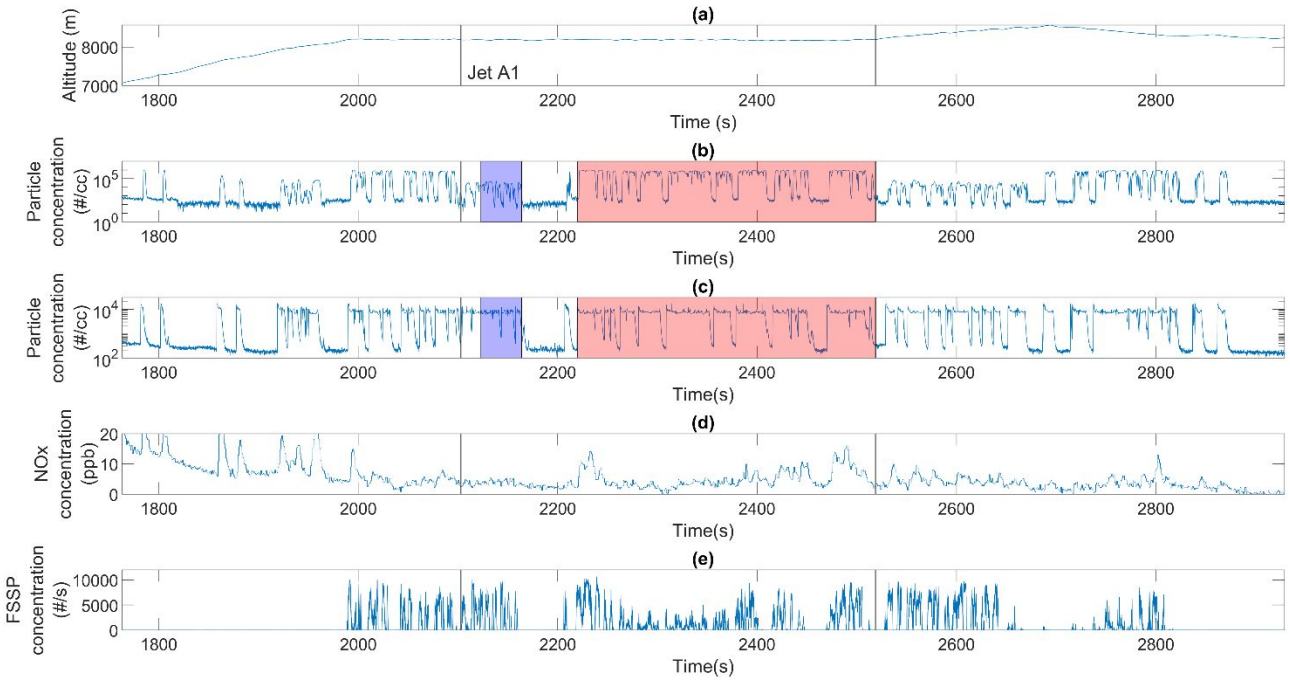

286

287 **Figure S13.** Raw data plot for the Jet A1 flight on Dec 21 with lines indicating the segments
288 chosen for analysis: (a) altitude measurements from the CT-133 (b) 3776 CPC particle
289 concentration, (c) 7610 CPC particle concentration, (d) NO_x concentration, (d) ice particle
290 concentration.

291

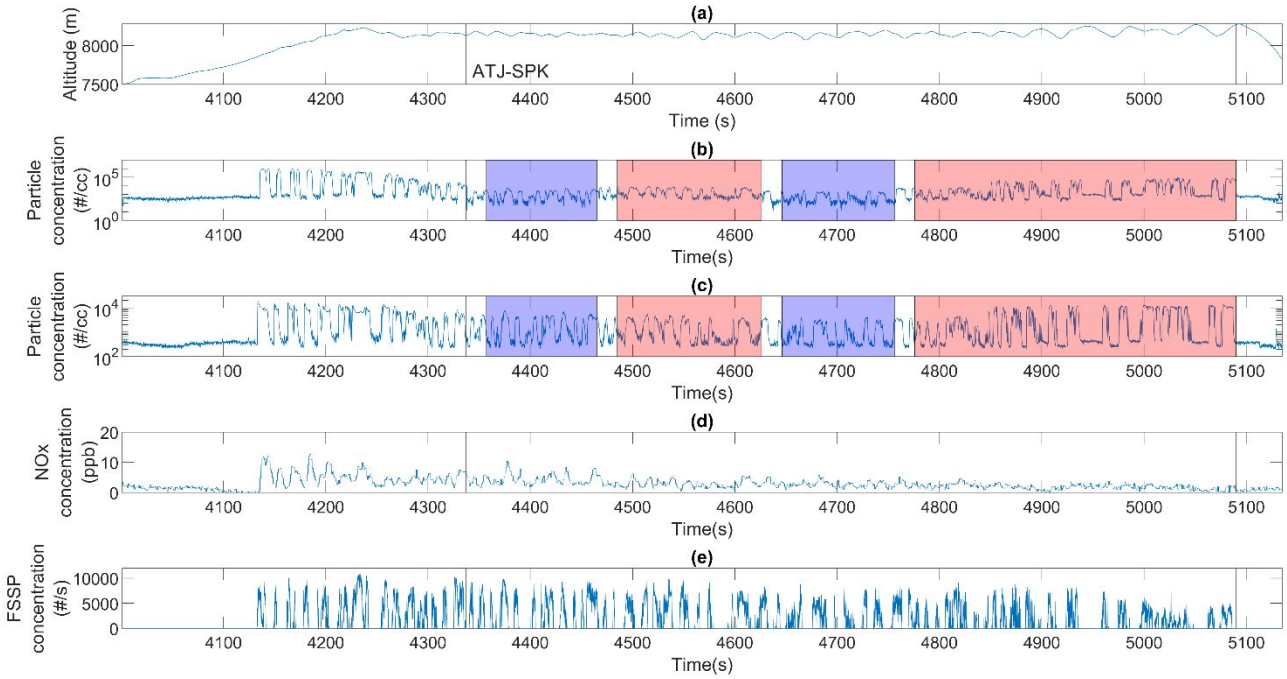

Figure S14. Raw data plot for the ATJ-SPK flight on Dec 21 with lines indicating the segments chosen for analysis: (a) altitude measurements from the CT-133 (b) 3776 CPC particle concentration, (c) 7610 CPC particle concentration, (d) NO_x concentration, (d) ice particle concentration.

S4 References used in the Supporting Information

(1) *Aerosol Measurement Principles, Techniques, and Applications*, 3rd ed.; Kulkarni, P., Baron, P. A., Willeke, K., Eds.; Wiley: Hoboken, N.J., 2011.

(2) Willeke, K. Temperature Dependence of Particle Slip in a Gaseous Medium. *Journal of Aerosol Science* **1976**, *7* (5), 381–387. https://doi.org/10.1016/0021-8502(76)90024-0.

(3) Pui, D. Y. H.; Romay-Novas, F.; Liu, B. Y. H. Experimental Study of Particle Deposition in Bends of Circular Cross Section. *Aerosol Science and Technology* **1987**, *7* (3), 301–315. https://doi.org/10.1080/02786828708959166.

(4) Catalytic Stripper Manual. Catalytic Instruments 2016.

(5) TSI. Model 3776 Ultrafine Condensation Particle Counter Operation and Service Manual. TSI Incorporated July 2011.

(6) Zhang, Z.; Liu, B. Y. H. Performance of TSI 3760 Condensation Nuclei Counter at Reduced Pressures and Flow Rates. *Aerosol Science and Technology* **1991**, *15* (4), 228–238. https://doi.org/10.1080/02786829108959530.

(7) Moore, R. H.; Thornhill, K. L.; Weinzierl, B.; Sauer, D.; D'Ascoli, E.; Kim, J.; Lichtenstern, M.; Scheibe, M.; Beaton, B.; Beyersdorf, A. J.; Barrick, J.; Bulzan, D.; Corr, C. A.; Crosbie, E.; Jurkat, T.; Martin, R.; Riddick, D.; Shook, M.; Slover, G.; Voigt, C.; White, R.; Winstead, E.; Yasky, R.; Ziemba, L. D.; Brown, A.; Schlager, H.; Anderson, B. E. Biofuel Blending Reduces Particle Emissions from Aircraft Engines at Cruise Conditions. *Nature* **2017**, *543* (7645), 411. https://doi.org/10.1038/nature21420.

(8) Zhang, X.; Chen, X.; Wang, J. A Number-Based Inventory of Size-Resolved Black Carbon Particle Emissions by Global Civil Aviation. *Nature Communications* **2019**, *10* (1), 534. https://doi.org/10.1038/s41467-019-08491-9.

(9) Takegawa, N.; Iida, K.; Sakurai, H. Modification and Laboratory Evaluation of a TSI Ultrafine Condensation Particle Counter (Model 3776) for Airborne Measurements. *Aerosol Science and Technology* **2017**, *51* (2), 235–245. https://doi.org/10.1080/02786826.2016.1261990.

(10) ASME. *PTC 19.1-2013 Test Uncertainty*; The American Sociert of Mechanical Engineers (ASME): New York, NY, 2013.

(11) Schulte P.; Schlager H.; Ziereis H.; Schumann U.; Baughcum S. L.; Deidewig F. NO x Emission Indices of Subsonic Long-range Jet Aircraft at Cruise Altitude: In Situ Measurements and Predictions. *Journal of Geophysical Research: Atmospheres* **1997**, *102* (D17), 21431–21442. https://doi.org/10.1029/97JD01526.